Corrosion Protection Behavior of Aluminate Ion-Loaded Layered Double Hydroxide Coating on AZ31 Magnesium Alloy

Sachiko Hiromoto[1, z], Kasumi Fukuzawa[2], Kotaro Doi[1], Makoto Chiba[1, 2] and Naofumi Ohtsu[3]

[1] Research Center for Structural Materials, National Institute for Materials Science, 305-0047 Tsukuba, Japan

[2] Department of Materials Chemistry, National Institute of Technology, Asahikawa College, 071-8142 Asahikawa, Japan

[3] Faculty of Engineering, Kitami Institute of Technology, 090-0015 Kitami, Japan

[z] Corresponding author: S. Hiromoto
E-mail Address [hiromoto.sachiko@nims.go.jp]

Abstract

Effect of aluminate ion loading on the corrosion behavior of layered double hydroxide (LDH) coating of Mg-3Al-1Zn (AZ31) alloy was investigated. The corrosion inhibition performance of $NaAlO_2$ for AZ31 was examined by immersion and polarization tests. Then, aluminate ion-loaded LDH ($LDHAlO_2$) was synthesized from hydrotalcite ($LDHCO_3$) and co-deposited with magnesium and aluminum double hydroxide on AZ31 by electrophoretic co-deposition. Polarization, electrochemical impedance (EI) and wet-dry cyclic corrosion tests were conducted on the $LDHAlO_2$- and $LDHCO_3$-coated specimens. Adding 10-50 mmol/L $NaAlO_2$ to 0.1 mol/L NaCl solution induced a clear passive region on the polarization curves of AZ31 and shifted the breakdown potential over -1.0 V (Ag/AgCl), indicating the corrosion inhibition property of $NaAlO_2$. In the polarization and EI tests, the aluminate ion loading did not noticeably enhance the corrosion protection ability of the LDH coating as shown by higher quasi-passive current density and lower R_p than without loading. However, in the wet-dry corrosion tests, the $LDHAlO_2$-coated AZ31 demonstrated less weight gain and fewer clusters of shallow micro-pits, while the $LDHCO_3$-coated AZ31 showed numerous deeper pits on the entire surface. It was revealed that loading aluminate ions to the LDH coatings is promising for enhancing their corrosion protection ability in atmospheric environments.

Introduction

Magnesium alloys are attractive light-weight materials for automobiles, aircrafts and so on [1, 2]. However, their practical use is limited by the low corrosion resistance. To overcome this issue, various anti-corrosion coatings such as phosphate-based and fluoride-based coatings have been developed by various coating methods such as chemical conversion, anodization and plating [3, 4].

As an anticorrosion coating for Mg and Al alloys, layered double hydroxide (LDH) coatings are one of the promising coatings. LDH consists of a stacking of basic layers of double hydroxides of divalent and trivalent metal ions, with various anions in the interlayer and shows an anion exchange property [5]. Due to the anion exchange property, LDH is expected to be a reservoir of corrosion inhibitors and/or an absorber of chloride ions [6]. Then, corrosion inhibitor-loaded LDH coatings have been developed for Mg and Al alloys and steels to enhance the corrosion protection ability and to add self-healing property [6-15]. The corrosion inhibitors such as MoO_4^{2-}, VO_3^-, WO_4^{2-}, phenyl phosphonic acid (PPA), 2-mercaptobenzothiazole (MBT) and 8-hydroxyquinoline (8HQ) were loaded to the LDH coatings [10-15]. Meanwhile, suitable anionic corrosion inhibitors for loading to LDH coatings are still in exploration. As a corrosion inhibitor for Mg alloys, Na_2MoO_4 Na_2SnO_3 and $NaVO_3$ have been proposed [16-21]. In addition to these, we expect $NaAlO_2$ and $KAlO_2$ to act as a corrosion inhibitor because the oxide film containing more than 4% Al shows high corrosion resistance for AZ series Mg alloys [22-24] and $KAlO_2$ in the electrolyte deposits to form $MgAl_2O_4$ in the anodic oxide film of Mg alloy [25].

To form the corrosion inhibitor-loaded LDH coatings, generally, LDH coatings with NO_3^- or CO_3^- ions in the interlayer ($LDHNO_3$ or $LDHCO_3$) are formed on the alloys by steam treatment, autoclaving, chemical conversion and electrochemical deposition, and then the interlayer NO_3^- or CO_3^- ions are exchanged with anionic inhibitors in aqueous solutions [7-15].

The electrophoretic co-deposition (EP-co-D) method enables the LDH particles, which are pre-loaded with various corrosion inhibitors, to deposit on a variety of metal surfaces together with metallic hydroxide [26-28]. We therefore employed the EP-co-D method and developed composite coatings of $LDHCO_3$ particles and magnesium and aluminum double hydroxide (Mg-Al-DH) on Mg-3Al-1Zn (AZ31) alloy [29]. Another finding of this previous study was that $LDHNO_3$ formed the bottom layer in the EP-co-D coating. Another finding was that submicron to micron pores were formed in the EP-co-D layer by H_2 gas generated by the electrolysis of

water in the 80vol% ethanol-20vol% water mixed electrolyte [29]. Recently, the water content of the electrolyte was decreased to 2.4vol% to reduce the pore formation [30].

The purpose of this study was to develop a corrosion inhibitor-loaded LDH coating on Mg alloys. In this study, first, the effect of $NaAlO_2$ on the corrosion of AZ31 was examined as a potential corrosion inhibitor by immersion and polarization tests. Then, aluminate ion-loaded LDH ($LDHAlO_2$) was synthesized. The $LDHAlO_2$ particles were electrodeposited on AZ31 together with Mg-Al-DH by EP-co-D. The corrosion protection behavior of the coatings was examined by polarization, electrochemical impedance (EI) and wet-dry cyclic corrosion tests because the wet-dry cyclic environment is similar to the service environment of structural materials.

Experimental

Immersion tests of AZ31 in NaCl solution with $NaAlO_2$

AZ31 (Al 2.9mass%, Zn 1.05mass%, Mn 0.41mass%, Si 0.01mass%, Fe 0.001mass%, Cu <0.01mass%, Ni <0.001mass%, Mg Bal.) magnesium alloy plates of 15×15 mm and 2 mm thick were used as a specimen. The surface was ground with SiC papers (PSI, USA) up to #1200 and ultrasonically rinsed in 2-propanol. The specimen surface was covered with Teflon™ tape, leaving a test surface of 1 cm^2.

For immersion tests, 0.1 mol/L NaCl (Fujifilm-Wako) with and without addition of 1 – 50 mmol/L $NaAlO_2$ (Fujifilm-Wako) were prepared. The as-polished AZ31 were immersed in 200 mL of the respective solutions at room temperature for 24 h. The pH of the respective solutions and the weight of the specimen were measured before and after the immersion. The appearance of the immersed specimen was observed using digital camera. The specimen immersed with $NaAlO_2$ was characterized using scanning electron microscope (SEM: Miniscope TM3030Plus, Hitachi) and X-ray photoelectron spectroscopy (XPS: PHI 5000 VersaProbe, ULVAC-PHI). In the XPS analysis, monochromatized Al Kα radiation ($h\nu$=1486.6 eV) was adopted as the X-ray source, and the pass energy of the spectrometer was set to 23.5 eV. The photoelectron take-off angle was 45° and the diameter of the X-ray probe was about 100 μm. The binding energies of all the spectra were referenced to the C 1s peak at 285 eV. The background subtraction was carried out using Shirley's method. Spectral deconvolution was carried out mathematically

using a Gaussian-Lorentzian function.

Polarization tests of AZ31 in NaCl solution with $NaAlO_2$

The surface of AZ31 plates of 15×15 mm was ground and covered with Teflon™ tape in the same manner as the specimen for the immersion tests. 200 mL of 0.1 mol/L NaCl with and without 10 or 50 mmol/L $NaAlO_2$ solutions at room temperature was used as electrolyte. The counter and reference electrodes were a platinum wire and a Ag/AgCl electrode, respectively. The specimen was immersed in the electrolyte for 0.5 h to stabilize the open circuit potential (OCP). Subsequently the potential of the specimen was swept from a 50 mV lower or higher potential than the stabilized OCP in anodic or cathodic direction, respectively, at a sweep rate of 1 mV/s, using potentiostat (Interface 1010, Gamry).

Synthesis of aluminate ion-loaded LDH

The loading of aluminate ion (AlO_2^- ion) to LDH was carried out by the reconstruction process [31, 32]. 5 g of $LDHCO_3$ particles ($Mg_6Al_2(OH)_{16}CO_3 \cdot 4H_2O$, hydrotalcite, Sigma Aldrich) with a diameter of about 1 μm was heated at 500°C for 1 h and about 3.2 g of the thermal decomposed LDH particles was obtained. Subsequently, the entire thermal-decomposed LDH powder were suspended in 200 mL of 0.24 mol/L $NaAlO_2$ solution for 24 h at room temperature with stirring in a sealed glass vessel. After the 24 h rehydration process, the suspension was filtered, rinsed with deionized water and dried at 100°C for about 1 h, and about 4.8 g of $LDHAlO_2$ powder was obtained. The as-synthesized $LDHAlO_2$ powder were characterized using X-ray diffraction (XRD: D2 Phaser, Bruker) with a tube voltage of 30 kV, a tube current of 10 mA, and an increment of 0.02 degrees. To examine the intercalation of aluminate ions into LDH, the interlayer water was reduced by heat treatment at 140°C for 10 h for the as-synthesized $LDHAlO_2$ and as-received $LDHCO_3$ powders, and then XRD measurements were performed. The as-synthesized $LDHAlO_2$ and as-received $LDHCO_3$ powders were also characterized using diffuse reflectance Fourier transform infrared spectroscopy (FTIR: IRTracer-100, Shimadzu) with a resolution of 4 cm^{-1}, confocal Raman microscope (inVia Reflex, Renishaw) with a laser of 532 nm wavelength irradiated through a 50 times objective lens, and SEM (Miniscope TM3030Plus, Hitachi) equipped with energy

dispersive X-ray spectroscopy (EDS: X-stream-2, Oxford) with an accelerating voltage of 15 kV, and the results are shown in the supplementary material. Aluminate ion release from $LDHAlO_2$ particles in air-exposed pure water was examined using aluminium ion test paper (Aluminium Check, ADVANTEC) and the results are shown in the supplementary material.

Composite coating of $LDHAlO_2$ or $LDHCO_3$ particles and Mg-Al DH by EP-co-D

AZ31 plates of 25×30 mm and 2 mm thick were used as a substrate. The surface was ground with SiC papers up to #1200 and ultrasonically rinsed in 2-propanol. Immediately before the EP-co-D treatment, the substrate was immersed in 0.25 mol/L $C_{10}H_{14}N_2Na_2O_8 \cdot 2H_2O$ (FUJIFILM Wako) solution for 10–20 sec to remove the air formed oxide film.

An electrolyte of 60 mmol/L $Mg(NO_3)_2 \cdot 6H_2O$ (FUJIFILM Wako) and 15 mmol/L $Al(NO_3)_3 \cdot 9H_2O$ (FUJIFILM Wako) in 2.4vol% water-2-Propanol was prepared. Subsequently, $LDHAlO_2$ or $LDHCO_3$ particles were suspended in the electrolyte at a concentration of 2wt%. The suspensions were stirred for several minutes and then ultrasonicated for longer than 0.5 h.

AZ31 and carbon plates were mounted in an electrochemical cell with a distance of 10 mm as the deposition (working) and counter electrodes, respectively. Immediately after immersing the electrodes in the suspension, a constant voltage of 100 V was applied between the electrodes for 60 s. The EP-co-D specimen was dried at 100°C for 1 h, and then ultrasonicated in 2-propanol for 60 s to remove weakly glued particles. The weight of the specimens was measured before and after the EP-co-D and ultrasonication. The appearance of the specimens was observed using digital camera and the surface and cross section were observed using SEM in backscattered electron mode. The surface was characterized using XRD and confocal Raman microscope. The AZ31 coated with $LDHAlO_2$ and $LDHCO_3$ particles was denoted as $LDHAlO_2$-coated and $LDHCO_3$-coated AZ31 specimens, respectively. The as-polished AZ31 was denoted as uncoated AZ31 in contrast to the coated AZ31.

Polarization and EI tests of $LDHAlO_2$- and $LDHCO_3$-coated AZ31

Anodic polarization and EI tests were carried out for the $LDHAlO_2$-coated, $LDHCO_3$-coated and uncoated AZ31 specimens using potentiostat (SP-50e, Biologic). The counter and reference electrodes were a platinum wire and a Ag/AgCl electrode, respectively. The specimen was exposed the test surface of 1 cm^2 and the surrounding area was coated with epoxy. 200 mL of

0.1 mol/L NaCl solution at room temperature was used as electrolyte. For the polarization tests, the specimen was immersed in the electrolyte for 0.5 h to stabilize OCP, and subsequently the potential of the specimen was swept from a 50 mV lower potential than the stabilized OCP in anodic direction at a sweep rate of 1 mV/s. For the EI tests, after the static immersion for 0.5 h, potential perturbation was applied with an amplitude of 5 mV at frequency from 10 MHz to 50 mHz and 5 points per decade. Equivalent electric circuits were assumed and curve-fitting for the measured EI spectra was performed to obtain the values of parameters in the circuits using ZView. Three EI tests were carried out for each specimen.

Wet-dry cyclic corrosion tests of LDHAlO$_2$- and LDHCO$_3$-coated AZ31

Wet-dry cyclic corrosion tests were carried out for the LDHAlO$_2$-coated, LDHCO$_3$-coated and uncoated AZ31 specimens. 0.3wt% NaCl-75% ethanol solution was dropped onto the 20 $\times$30 mm test surface to place 1 g/m^2 NaCl. Then, the relative humidity around the specimens was controlled with one cycle of 8 h at 30%RH, 8 h at 95%RH and 8 h at 30%RH again at room temperature, and 14 cycles were repeated. The weight of the specimens before and after the corrosion tests was measured for three samples from each specimen. The appearance of the specimens was observed using digital camera and the surface and cross section was observed using SEM. The surface was characterized using XRD. The coatings in the apparently uncorroded area were analyzed using laser Raman spectroscopy. The corrosion products and the coatings were chemically removed from one corroded sample from each specimen using chromate-AgNO$_3$ solution and the surface topography and morphology were observed using one-shot 3D microscope (VR-3100, Keyence) and SEM.

Results

Immersion tests of AZ31 in NaCl with NaAlO$_2$

Figure 1 shows the appearance of the as-polished AZ31 surface immersed in the 0.1 mol/L NaCl solution with and without NaAlO$_2$, and a back-scattered electron SEM image of the surface immersed with 50 mmol/L NaAlO$_2$. The weight gain of the specimens and the pH of the solutions before and after immersion are shown in Fig. 2. The weight of Mg alloys generally increases by corrosion due to the formation of corrosion products such as Mg(OH)$_2$. As the

change in surface morphology was evident and the effect of $NaAlO_2$ was clear in the following polarization tests, weight measurements after removal of the corrosion products were not carried out.

In the NaCl-only solution, about half of the surface area shows black filiform corrosion, and the entire surface is covered by a white corrosion product (Fig. 1(a)). The weight of the specimen increases (Fig. 2), and the solution pH increases from 6.1 to 9.2. The weight gain in the NaCl-only solution shows large variation, which is due to the loss of some of the corrosion products during rinsing and drying.

The addition of 1 mmol/L $NaAlO_2$ decreases the filiform corrosion area (Fig. 1(b)). No obvious corrosion is observed with 10 and 50 mmol/L $NaAlO_2$ (Fig. 1(c) and (d)). The SEM image with 50 mmol/L $NaAlO_2$ shows no obvious corrosion except for dark contrast spots of 5-30 μm mainly around Al-Mn inclusions (bright contrast grains) (Fig. 1(e)). The weight gain decreases with an increase of $NaAlO_2$ addition (Fig. 2). The pH of the NaCl solution with 1-50 mmol/L $NaAlO_2$ is 9.6, 10.9 and 11.7, respectively, which does not significantly change after the immersion.

Figure 3(a) shows the XPS survey spectra of the AZ31 specimen as-polished and immersed with 10 and 50 mmol/L $NaAlO_2$. The photoelectron peaks from magnesium (Mg), aluminum (Al), silicon (Si), chlorine (Cl), oxygen (O), and carbon (C) are observed. Cl is derived from contaminated or residual NaCl.

Figure 3(b)-(e) shows the XPS narrow spectra of the C 1s, O 1s, Al 2p, Mg 2p and Zn 2p3 regions. The C 1s spectra (Fig. 3(b)) are decomposed into two peaks originating from C-C bond and carbonate. The carbonate peak is derived from magnesium carbonate formed from atmospheric CO_2. The O 1s spectra (Fig. 3(c)) are decomposed into two peaks from MgO and Al_2O_3+$Mg(OH)_2$. The MgO peak position is shifted by about 0.5 eV after immersion compared to that of the as-polished AZ31, which is attributed to the effect of adsorbed water.

The Al 2p spectra (Fig. 3(d)) of the AZ31 immersed with $NaAlO_2$ show a peak from Al_2O_3, and that of the as-polished AZ31 is decomposed into peaks from metallic Al and Al_2O_3. The intensity of Al_2O_3 peak of the specimens with $NaAlO_2$ is significantly higher than that of the as-polished AZ31, indicating that an Al_2O_3 film is formed in the solution with $NaAlO_2$. The Mg 2p spectrum (Fig. 3(e)) of the as-polished AZ31 is decomposed into two peaks from

metallic Mg and MgO and/or $Mg(OH)_2$, while that with $NaAlO_2$ shows a peak from MgO and/or $Mg(OH)_2$. The intensity of the Mg 2p spectra of the specimens with $NaAlO_2$ is lower than that of the as-polished AZ31, indicating a decrease in the magnesium fraction in the surface oxide film. Although the C 1s spectra indicates the presence of slight amount of $MgCO_3$, no distinct peak from $MgCO_3$ is observed in Mg 2p spectra. The Zn 2p3 spectra (Fig. 3(f)) of the specimens with $NaAlO_2$ show a peak derived from zinc oxide, while that of the as-polished AZ31 does not show any peak. These results indicate that after immersing in the NaCl solution with $NaAlO_2$, a relatively thick Al_2O_3 film with a small fraction of $MgO/Mg(OH)_2$ was formed.

Polarization tests of AZ31 in NaCl with $NaAlO_2$

Figure 4 shows the anodic and cathodic polarization curves of AZ31 in the 0.1 mol/L NaCl solution with and without $NaAlO_2$. The anodic polarization curves show a constant current density and a breakdown potential. The constant current density decreases by 100 times to be a passive current density of 3×10^{-7} $A\cdot cm^{-2}$ with 10 and 50 mmol/L $NaAlO_2$. The breakdown potential drastically increases from -1.35 V (vs. Ag/AgCl) to -1.15 V with 10 mmol/L $NaAlO_2$. No breakdown potential appears in the potential region to -1.0 V with 50 mmol/L $NaAlO_2$. The cathodic current density decreases by 100 times with $NaAlO_2$. It is demonstrated that $NaAlO_2$ suppresses the cathodic and anodic reactions on AZ31.

Synthesis of aluminate ion-loaded LDH

Figure 5 shows the wide-range XRD patterns of the as-synthesized $LDHAlO_2$ and as-received $LDHCO_3$ powders and the 140°C-treated $LDHAlO_2$ and $LDHCO_3$ powders, and the magnified diffraction peaks from LDH 003 plane ($(003)_{LDH}$). The as-received and 140°C-treated $LDHCO_3$ powders show a typical XRD pattern of LDH structure of hydrotalcite (JCPDS card 22–700). The as-synthesized and 140°C-treated $LDHAlO_2$ powders show broad diffraction peaks from LDH structure with relatively low intensity, small diffraction peaks from $Al(OH)_3$ (boehmite) [33] and a slight peak from thermally decomposed LDH. $Al(OH)_3$ is insoluble in aqueous solutions at room temperature. Thus, the as-synthesized $LDHAlO_2$ powder was used for the EP-co-D.

The position of the $(003)_{LDH}$ peak of the as-synthesized $LDHAlO_2$ is 11.52 degrees which is similar to 11.56 degrees of $LDHCO_3$ (Fig. 5(b)). The intercalation of aluminate ions to

$LDHAlO_2$ could not be determined from this peak position. The 140°C-treatment shifts the $(003)_{LDH}$ peak of the $LDHAlO_2$ to the higher angle side of 12.25 degrees, whereas that does not change the $(003)_{LDH}$ peak position of the $LDHCO_3$.

Composite coating of $LDHAlO_2$ or $LDHCO_3$ particles and Mg-Al-DH

Figure 6 shows the optical and SEM images of the surface of the $LDHAlO_2$- and $LDHCO_3$-coated AZ31 specimens after ultrasonication. The $LDHAlO_2$ and $LDHCO_3$ coatings cover the surface uniformly (Fig. 6(a) and (b)) but show cracking under SEM observation (Fig. 6(c) and (d)). The weight of the $LDHAlO_2$ coating was 6.8±0.9 mg that was smaller than 8.2±1.4 mg of the $LDHCO_3$ coating. The magnified SEM images of the coatings show that LDH particles are glued with gel-like dark contrast substance, which was attributed to Mg-Al-DH by the following XRD analysis (Fig. 6(e) and (f)). A tiny amount of $Al(OH)_3$ needle-shaped particles is deposited in the $LDHAlO_2$ coating. The magnified SEM images of the substrate exposed inside coating cracks show that the gel-like Mg-Al-DH and LDH particles densely cover the substrate surface (Fig. 6(g) and (h)).

Figure 6(i) and (j) shows the cross section of the $LDHAlO_2$- and $LDHCO_3$-coated AZ31 specimens after ultrasonication. The thickness of the coating layer was not uniform, and the coating in Fig. 6(i) appears thicker than in (j), but this does not necessarily the case for the entire coating. The cross-sectional SEM images show that the $LDHAlO_2$ coating is coarser than the $LDHCO_3$ coating (Fig. 6(i) and (j)). The $LDHCO_3$ coating shows that the gel-like Mg-Al-DH deposits preferentially at the bottom of the coating to form a dense inner layer (Fig. 6 (j)) as previously reported [29]. Such a preferential deposition of the gel-like Mg-Al-DH at the bottom of the $LDHAlO_2$ coating is not significant on the cross-sectional image, but the formation of the thin dense inner layer is suggested by the surface observation (Fig. 6(i) and (g)).

Figure 7(a) shows the wide-range XRD patterns of the $LDHAlO_2$- and $LDHCO_3$-coated AZ31 specimens after ultrasonication. The diffraction peaks from LDH and substrate AZ31 are observed for both specimens, and a very small peak from γ-$Al(OH)_3$ is observed for the $LDHAlO_2$-coated AZ31. Additionally, broad peaks are observed at around 18−19 degrees and 32−40 degrees which correspond to 18.649 degrees and 38.0154 degrees of brucite $Mg(OH)_2$ (JCPDS card No. 00-44-1482), respectively. The magnified $(003)_{LDH}$ peaks (Fig. 7(b)) are

asymmetrical owing to a shoulder peak on the lower angle side which is attributed to $LDHNO_3$ as reported in our previous work [29]. Formation of $LDHNO_3$ is also suggested by the result that it was formed in the $Mg(NO_3)_2$ and $Al(NO_3)_3$ electrolyte without LDH particles by electrodeposition as shown in Fig. S3. Thus, the gel-like substance with dark contrast in the SEM images (Fig. 6) was attributed to Mg-Al-DH with brucite structure, which should have been a precursor to $LDHNO_3$.

Polarization and EI behavior of $LDHAlO_2$- and $LDHCO_3$-coated AZ31

Figure 8(a) shows the anodic polarization curves of the LDH-coated and uncoated AZ31 specimens in the 0.1 mol/L NaCl solution. The $LDHAlO_2$- and $LDHCO_3$-coated AZ31 specimens show a quasi-passive current density of about 1×10^{-5} A cm^{-2} and 5×10^{-6} A cm^{-2}, respectively. These are less than half of the constant current density of 3×10^{-5} A cm^{-2} of the uncoated AZ31. The breakdown of the $LDHAlO_2$- and $LDHCO_3$-coated AZ31 surfaces does not occur in this potential range up to -1 V.

Figure 8(b) and (c) shows the Nyquist and Bode plots of EI spectra of the LDH-coated and uncoated AZ31 specimens in the 0.1 mol/L NaCl solution. The LDH-coated AZ31 specimens apparently show one capacitive semi-circle on the Nyquist plots and one peak at around 40 Hz on the phase shift curves, so an equivalent electric circuit shown in Fig. 8(d) was assumed. R_s represents the solution resistance. R_{coat} and CPE_{coat} represent the resistance and constant phase element (*CPE*) of the LDH coatings, respectively. The *CPE* was used instead of the capacitance due to the porous structure of the LDH coatings. The uncoated AZ31 shows two semi-circles on the Nyquist plot and two peaks at around 80 Hz and 2×10^{-1} Hz on the phase shift curves, so an equivalent circuit shown in Fig. 8(e) was assumed. The magnified 2×10^{-1} Hz peak is shown as an inset in Fig. 8(c). R_{film} and CPE_{film} represent the resistance and of the surface oxide film, respectively. R_{ct} and CPE_{dl} represent the charge transfer resistance and *CPE* of electric double layer, respectively. Curve fitting was performed, and the fitted curves are shown in Fig. 8(b) and (c). The obtained corrosion parameters are summarized in Table 1. The polarization resistance (R_p) of the uncoated AZ31 was estimated using the Eq. (1) and shown in Table 1 and Fig. 8(f).

$$\frac{1}{R_p} = \frac{1}{R_{film}+R_{ct}} \quad (1)$$

The R_p of the LDH-coated AZ31 specimens is more than twice as high as that of the uncoated AZ31. The R_p of the LDHAlO_2-coated AZ31 is slightly lower than that of the LDHCO_3-coated AZ31. The R_{coat} values of the LDH-coated specimens are higher than the R_{film} of the uncoated specimen. The *CPE*-T values, roughly corresponding to capacity of the surface layer, are comparable for the LDH-coated and uncoated AZ31 specimens and the *CPE*-P values are similar between the specimens.

Wet-dry cyclic corrosion behavior of LDHAlO_2- and LDHCO_3-coated AZ31

Figure 9 shows the weight gain of the LDH-coated and uncoated AZ31 specimens after the wet-dry cyclic corrosion tests. The weight measurement after removal of the coating and corrosion products was not performed because the difference in the weight gain and corrosion morphology between specimens was evident. The weight gain of the LDH-coated AZ31 specimens is significantly smaller than the uncoated AZ31, and that of the LDHAlO_2-coated AZ31 is smaller than that of the LDHCO_3-coated AZ31.

Figure 10(a)-(f) shows the optical images of the specimens after the corrosion tests. Figure 10(g) and (h) shows the SEM images of the white dots arrowed in the optical images and reveals that the dots are corrosion sites or pits. Almost the entire surface of the uncoated AZ31 is colored in brown and covered with micrometer-sized corrosion pits, and some of them grow to millimeter-sized pits (Fig. 10(f)). The LDHAlO_2-coated AZ31 shows small number of micrometer- to millimeter-sized corrosion sites (Fig. 9(a) and (d)), and the LDHCO_3-coated AZ31 shows a lot of micrometer-sized corrosion pits on the entire surface (Fig. 9(b) and (e)).

Figure 10(i) and (j) shows the magnified coating layer in apparently uncorroded area. Figure 10(k) and (l) shows the cross-sectional SEM images. The LDHAlO_2 coating in the apparently uncorroded area remains almost original morphology. Both the LDH coatings show amorphous substance between particles, and the amount of amorphous substance deposited in the LDH AlO_2 coating appears to be smaller than that in the LDHCO_3 coating.

Figure 11 shows the wide-range XRD patterns and magnified $(003)_{LDH}$ peak of the specimens after the corrosion tests. The corroded LDHAlO_2-coated AZ31 shows diffraction peaks from LDH and substrate AZ31, and no obvious peaks from corrosion products are observed. The corroded LDHCO_3-coated AZ31 shows peaks from LDH, substrate AZ31 and a

corrosion product of dypingite ($Mg_5(CO_3)_4(OH)_2 \cdot 5H_2O$). The corroded uncoated AZ31 shows broad peaks from LDH and dypingite in addition to those from substrate AZ31. The position of $(003)_{LDH}$ peak of the corroded LDH-coated specimens is 11.60 degrees which does not apparently change from that of the as-coated specimens (Fig. 7).

To examine the change of the interlayer anions of LDH due to corrosion, the coatings before and after the corrosion tests were analyzed using Raman spectrometer. The vibrational region of interlayer anions from 1000 to 1150 cm^{-1} [34-37] is shown in Fig. 12. For the specimens after the corrosion tests, the coatings in a visually uncorroded area were analyzed. The area without needle-shaped particles was defined as the analysis area for the $LDHAlO_2$ coating.

The $LDHAlO_2$ coating after the corrosion test shows a peak at 1051 cm^{-1}, a tiny peak at 1067 cm^{-1} and a broad peak at 1101 cm^{-1}, while the as-prepared $LDHAlO_2$ coating shows a relatively large peak at 1045 cm^{-1} and broad shoulder peaks at around 1058 cm^{-1} and small peaks at 1088 and 1109 cm^{-1}. The peak at 1045 cm^{-1} is generally attributed to interlayer NO_3^- ions of LDH [38]. The peak at around 1060 cm^{-1} is presumably attributed to interlayer AlO_2^- and CO_3^{2-} ions, as the peak at around 1060 cm^{-1} is attributed to the symmetric stretching vibrations of interlayer CO_3^{2-} ions of Mg-Al-$LDHCO_3$ [34-37] and the peaks near 1056 and 1068 cm^{-1} are attributed to Al-O bending mode of γ-$Al(OH)_3$ [39, 40]. The peaks at 1087 and around 1100 cm^{-1} are attributed to free CO_3^- ions [37] and CO_3^{2-} symmetric stretching vibrations in magnesite ($MgCO_3$) [37], respectively. The relative intensity of the 1045 and 1060 cm^{-1} peaks to the 1085 and 1100 cm^{-1} peaks decreases after the corrosion test, indicating that the interlayer NO_3^- and AlO_2^- ions were exchanged with CO_3^{2-} ions.

The $LDHCO_3$ coating after the corrosion shows the peaks at 1050, 1063, 1090 and 1122 cm^{-1}. The as-prepared $LDHCO_3$ coating shows the peaks at 1045, 1061 and 1086 cm^{-1}. The relative intensity of the 1045 cm^{-1} peak to the 1060 cm^{-1} peak decreases after the corrosion, indicating the anion exchange between interlayer NO_3^- and CO_3^{2-} ions. The 1123 cm^{-1} peak is attributed to CO_3^{2-} stretching vibrations in dypingite [36, 41].

Figure 13 shows the optical, SEM and topography images and the corresponding line profiles after removing the coatings and corrosion products. The corrosion site and pit arrowed in Fig. 13(a) and (b) corresponds to those in the SEM images of Fig. 13(c) and (d), respectively and to the white dots arrowed in Fig. 10(a) and (b), respectively. The $LDHAlO_2$-coated AZ31 in Fig. 10(a) shows several corrosion sites with a diameter of 0.5-1.5 mm where a lot of shallow

micro-pits with a depth of a few micrometers are clustered as shown in Fig. 13(a), (c), (e) and (g). Outside of the micro-pits clustering areas, almost no corrosion is observed as shown in Fig. 13(e). The $LDHCO_3$-coated AZ31 in Fig. 10(b) shows many micro-pits on the entire surface and sometimes shows larger pits with a depth of about 10 μm as shown in Fig. 13(b), (d), (f), (h) and (i).

Discussion

Synthesis of $LDHAlO_2$ by reconstruction process

The addition of $NaAlO_2$ in NaCl solution led to the formation of a relatively thick Al_2O_3 film on AZ31 and the significant improvement of the corrosion resistance of AZ31 as shown by the decrease in weight gain in the immersion tests and the clear passive region on the polarization curves (Figs. 1-4). These facts demonstrated the corrosion inhibition property of $NaAlO_2$. Therefore, aluminate ions were loaded to LDH as a corrosion inhibitor.

The as-synthesized $LDHAlO_2$ showed the $(003)_{LDH}$ diffraction peak at almost the same position as the as-received $LDHCO_3$ (Fig. 5). However, the intercalation of aluminate ions into the synthesized $LDHAlO_2$ cannot be denied solely by the XRD measurements because the $(003)_{LDH}$ peak position depends not only on the type of the interlayer anions but also on the orientation of the interlayer anions [42]. Other anions that could be present at the interlayer of LDH besides aluminate ions are CO_3^{2-} and OH^- ions. The presence of CO_3^{2-} ions was suggested by the Raman results, so that the as-synthesized $LDHAlO_2$ powder could contain $LDHCO_3$. In the case of LDH hydroxide with interlayer OH^- ions, the $(003)_{LDH}$ peak was shifted by 250°C-treatment but recovered its original position in a few minutes in air [43]. On the other hand, the $(003)_{LDH}$ peak position of the as-synthesized $LDHAlO_2$ irreversibly shifted by the 140°C-treatment, indicating that the interlayer anions were not OH^- ions.

As mentioned above, the position shift of the $(003)_{LDH}$ diffraction peak of $LDHAlO_2$ to the higher angle after the 140°C-treatment (Fig. 5) indicated that anions other than CO_3^{2-} and OH^- ions were intercalated into the as-synthesized $LDHAlO_2$ and these are circumstantially aluminate ions. It was reported that the interlayer water in the Mg-Al- and Mg-Fe-LDH desorbed over 130°C [44]; however, the loss of interlayer water did not lead to the change in XRD pattern of LDH [45]. Thus, the position shift of the $(003)_{LDH}$ peak was not attributed to the desorption of interlayer water.

The interlayer spacing of the $LDHAlO_2$ decreased by the 140°C-treatment. Then, during the heat treatment at 140°C, it is supposed that the reactions between aluminate ions (AlO_2^-) and interlayer water described in Eq. (2) and (3) occur at the interlayer.

$$(AlO_2^-)_{interlayer} + 2(H_2O)_{interlayer} \rightarrow Al(OH)_3 + OH^- \quad (2)$$

$$(AlO_2^-)_{interlayer} + (H_2O)_{interlayer} \rightarrow AlO(OH) + OH^- \quad (3)$$

According to the EDS analysis of the as-synthesized $LDHAlO_2$ and as-received $LDHCO_3$ powders, the relative atomic concentration ratio of Mg to Al of the $LDHAlO_2$ was 1.7±0.0 which was lower than 2.1±0.0 of the $LDHCO_3$ (Fig. S1 and Table S1 in supplementary material). The Raman spectra of the as-synthesized $LDHAlO_2$ and the $LDHAlO_2$ coating showed the peak being attributed to Al-O bending mode although this peak was also attributed to CO_3^{2-} ions (Fig. S3 and Fig. 12(a)). These results indicate that aluminate ions were loaded to LDH either at the interlayer and/or outer surface. From the whole, it was presumed that the synthesized $LDHAlO_2$ powder was a mixture of LDH with aluminate ions at the interlayer and outer surface, $LDHCO_3$ and the thermally decomposed LDH.

Formation of $LDHAlO_2$ and Mg-Al-DH composite coating

The composite coating of $LDHAlO_2$ or $LDHCO_3$ particles and Mg-Al-DH was formed by the EP-co-D in the similar manner to the previous work [29]. The $LDHAlO_2$ coating was coarser than the $LDHCO_3$ coating as shown in Fig. 6(i) and (j). This is presumably because the $LDHAlO_2$ particles agglomerated during the rehydration procedure which disturbed the dense deposition of LDH particles. However, the reasons for the difference in the coating morphology depending on the composition of LDH are a future subject.

The deposition of Mg-Al-DH with low crystallized brucite structure was shown by the broad diffraction peaks around 18 and 35 degrees (Fig. 7) corresponding to brucite. The amount of Mg-Al-DH appeared to be smaller in the $LDHAlO_2$ coating than in the $LDHCO_3$ coating, which is indicated by the cross-sectional observation and the smaller coating weight. However, the Mg-Al-DH covered the substrate surface with LDH particles as shown at the crack bottom of the coatings (Fig. 6), and the coatings could show the corrosion protection performance. A part

of the Mg-Al-DH with brucite structure should have been transformed to $LDHNO_3$ as indicated by the shoulder peak at lower angle side of the $(003)_{LDH}$ diffraction peak, the Raman peak at 1045 cm^{-1} [38] (Fig. 7 and 12), and the $LDHNO_3$ formation in the electrolyte without LDH particles (Fig. S8). The $LDHNO_3$ could be formed at the bottom of the coating, since the $LDHNO_3$ was present at the bottom of the composite coating formed in the suspension with higher portion of water [29].

Corrosion protection ability of $LDHAlO_2$ and Mg-Al-DH composite coating in aqueous solution

In the polarization and EI tests in the aqueous solution (Fig. 8), the LDH coatings exhibited the barrier property as shown by the decrease in the constant current density, the suppression of the surface breakdown in the potential range up to -1 V and the higher R_p, in comparison to the uncoated AZ31.

The Nyquist and Bode plots of the LDH-coated AZ31 specimens showed the presence of one time constant (Fig. 8(b) and (c)). The LDH-coated and uncoated specimens showed the comparable *CPE*-T values, but the R_{coat} values of the LDH-coated specimens were higher than the R_{film} of the uncoated specimen. These results indicate that the layer that exhibited capacitive property in the LDH coatings was qualitatively different from that on the uncoated surface. Here, the LDH coatings showed a dense inner layer consisting of mainly Mg-Al-DH, $LDHNO_3$, and LDH particles (Figs. 6 and 7), which presumably exhibited capacitive property. The $LDHAlO_2$ coating with the thinner inner layer showed the higher quasi-passive current density and the lower R_p than the $LDHCO_3$ coating with the thicker inner layer (Figs. 6 and 8). These facts indicate that the barrier property of the LDH coatings depended on the dense Mg-Al-DH inner layer. Also, it is suggested that the composite coatings can be thinned to show corrosion protection.

The suppression of the LDH coating breakdown can be attributed to the Cl^- absorption of $LDHAlO_2$ and $LDHNO_3$ by anion-exchange in addition to the barrier property of the coatings. The anion exchange between Cl^- and NO_3^- ions of $LDHNO_3$ can be expected because the order of anion selectivity of LDH is determined approximately by the magnitude of the charge density of the anions and the ion-exchange equilibrium constant of Cl^- ion is higher than that of NO_3^- ion [46].

Here, the quasi-passive current density of the LDH-coated AZ31specimens was higher than that of the as-polished AZ31 in $NaAlO_2$-added NaCl solution (Fig. 4 and 8(a)), indicating that the barrier property of the LDH coatings was lower than the Al_2O_3 film formed by AlO_2^- ion adsorption. The Al_2O_3 film was thinner but less defective than the LDH coatings. It was found that the coating with less defects can exhibit higher barrier ability than the defective coating in short duration tests like the polarization test.

Corrosion protection ability of LDHAlO_2 and Mg-Al-DH composite coating in atmospheric corrosion environment

In the wet-dry cyclic corrosion tests, the LDH coatings significantly suppressed the corrosion of AZ31 as can be seen from the remarkable decrease in the weight gain and the much fewer corrosion sites comparing to the uncoated AZ31 (Figs. 9, 10 and 13). Furthermore, the higher corrosion protection ability of the LDHAlO_2 coating than the LDHCO_3 coating was demonstrated by the smaller weight gain and the smaller number of corrosion sites with the shallower corrosion pits (Figs. 9, 10 and 13). No corrosion was observed outside of the corrosion sites on the LDHAlO_2-coated AZ31 (Figs. 10 and 13). The smaller number of corrosion sites of the LDHAlO_2-coated AZ31 suggests the anion exchange between Cl^- and aluminate ions of LDHAlO_2 [5, 46] suppressed the corrosion initiation and/or promptly repaired the initiating corrosion pits. The anion exchange between Cl^- and NO_3^- ions of LDHNO_3 should also have contributed to the suppression of the corrosion initiation, which was common to the LDHAlO_2 and LDHCO_3 coatings. Therefore, the corrosion mechanisms shown in Fig 14 are assumed for the LDHAlO_2- and LDHCO_3-AZ31 specimens under the wet-dry cyclic corrosion tests. The details of the role of the anion exchange property of LDHAlO_2 in repairing corrosion sites is a matter for further study. When the specimens were wet, corrosion initiated by Cl^- ions at defects in the LDH coatings and corrosion products precipitated. The corrosion initiation of the LDHAlO_2-coated AZ31 was suppressed because a part of Cl^- ions were absorbed by LDHAlO_2 and LDHNO_3 by the anion exchange. Then, the released aluminate ions could precipitate with the corrosion products and repaired the initiating corrosion pits. On the LDHCO_3-coated AZ31, corrosion initiated more frequently and the initiated corrosion pits could grow. When the specimens were dry, the corrosion products with and without aluminate ions were matured to show a certain corrosion protectiveness.

Conclusions

The effect of aluminate ion loading on the corrosion protection property of the LDH coating was investigated. The corrosion inhibition performance of $NaAlO_2$ on AZ31 was investigated as a potential corrosion inhibitor by the immersion and polarization tests and XPS analysis. Aluminate-ion loaded LDH ($LDHAlO_2$) was synthesized from $LDHCO_3$ by the reconstraction process and co-deposited with Mg-Al-DH on AZ31 by the EP-co-D method. The corrosion behavior of the $LDHAlO_2$- and $LDHCO_3$-coated AZ31 specimens was examined by the polarization, EI and wet-dry cyclic corrosion tests. The following findings were derived.

1) $NaAlO_2$ showed corrosion inhibition property for AZ31 by forming the Al_2O_3 film at the addition of 10 mmol/L or more in the 0.1 mol/L NaCl solution. The addition of 50 mmol/L $NaAlO_2$ decreased the constant current density by a factor of 100 and significantly shifted the breakdown potential from -1.35 V to over -1.0 V.

2) The composite coatings of $LDHAlO_2$ or $LDHCO_3$ particles and Mg-Al-DH showed a dense inner layer consisting of mainly Mg-Al-DH, LDH particles and $LDHNO_3$. The dense inner layer of the $LDHAlO_2$ coating was thinner than that of the $LDHCO_3$ coating.

3) The $LDHAlO_2$ and $LDHCO_3$ coatings showed a barrier property due to the dense inner layer in the polarization and EI tests in the 0.1 mol/L NaCl solution. The LDH-coated AZ31 specimens exhibited the constant current density less than half of the uncoated AZ31 and more than double the R_p. The LDH-coated AZ31 specimens did not show breakdown on the polarization curves in the potential region up to -1.0 V.

4) The $LDHAlO_2$-coated AZ31 showed higher corrosion resistance than the $LDHCO_3$-coated AZ31 in the wet-dry cyclic corrosion tests. The former showed the weight gain less than half of the latter, and the corrosion pits were fewer and shallower. The aluminate ion loading to LDH coating was effective to enhance the corrosion protection ability of the LDH coatings in the atmospheric environment.

Acknowledgments

This work was partially supported by the NIMS internship program and by the NIMS Molecule & Material Synthesis Platform in the Nanotechnology Platform Project of National Institute for Materials Science (NIMS). Ms. Nishikawa and Ms. Inokuma are acknowledged

for their sincere support during the experiments. The authors are grateful to Dr. Uchikoshi at NIMS for his valuable advice on electrophoretic deposition method.

References

1. J. Hillis, in *Magnesium Technology, Metallurgy, Design Data, Applications*, H. E. Friedrich and B. L. Mordike, eds., p. 469-498, Springer-Verlag, Berlin, (2006).
2. E. Sato, in *Handbook of Advanced Magnesium Technology*, The Japan Magnesium Association, ed., p. 71-104, Kallos, Tokyo, (2000).
3. M. Hino, *Journal of The Surafce Finishing Society of Japan,* **71** (3), 205-211 (2020).
4. S. Namba, *J. Surf. Finish. Soc. Jpn.,* **71** (3), 219-223 (2020).
5. T. Hibino, *Journal of The Clay Science Society of Japan,* **45** (2), 102-109 (2006).
6. K. Nakamura, M. Tsunakawa, Y. Shimada, A. Serizawa, and T. Ishizaki, *Surface and Coatings Technology,* **328** 436-443 (2017).
7. T. Ishizaki, S. P. Cho, and N. Saito, *Crystengcomm,* **11** (11), 2338-2343 (2009).
8. N. Kamiyama and T. Ishizaki, *Journal of The Japan Institute of Light Metals,* **64** (12), 638-642 (2014).
9. F. G. Wu, J. Liang, Z. J. Peng, and B. X. Liu, *Applied Surface Science,* **313** 834-840 (2014).
10. K. A. Yasakau, A. Kuznetsova, S. Kallip, M. Starykevich, J. Tedim, M. G. S. Ferreira, and M. L. Zheludkevich, *Corrosion Science,* **143** 299-313 (2018).
11. T. T. Wen, R. Yan, N. Wang, Y. X. Li, T. Chen, and H. Y. Ma, *Surface and Coatings Technology,* **383** 125255 (2020).
12. T. Hu, Y. J. Ouyang, Z. H. Xie, and L. Wu, *Journal of Materials Science & Technology,* **92** 225-235 (2021).
13. L. Wu, X. X. Ding, Z. Zheng, A. Tang, G. Zhang, A. Andrej Atrens, and F. S. Pan, *Journal of Materials Scienc & Technology,* **61** 66-72 (2021).
14. J. K. E. Tan, N. Birbilis, S. Choudhary, S. Thomas, and P. Balan, *Corrosion Science,* **205** 110444 (2022).
15. B. Pillado, B. Mingo, R. del Olmo, E. Matykina, A. M. Kooijman, Y. Gonzalez-Garcia, R. Arrabal, and M. Mohedano, *Journal of Magnesium and Alloys,* **11** (1), 201-216 (2023).
16. S. V. Lamaka, B. Vaghefinazari, D. Mei, R. P. Petrauskas, D. Hoche, and M. L. Zheludkevich, *Corrosion Science,* **128** 224-240 (2017).
17. M. A. Osipenko, D. A. Kharytonau, A. A. Kasach, J. Ryl, J. Adamiec, and I. I. Kuriklo, *Electrochimca Acta,* **414** 140175 (2022).

18. D. S. Kharitonov, M. Zimowska, J. Ryl, A. Zielinski, M. A. Osipenko, J. Adamiec, A. Wrzesinska, P. M. Claesson, and I. I. Kurilo, *Corrosion Science,* **190** 109664 (2021).

19. Z. Feng, J. Li, Z. Yang, and R. Buchheit, *Materials (Basel),* **13** (6), 1325 (2020).

20. L. Chen, X. Ma, Z. Ma, D. Lu, and B. Hou, *Royal Society of Chemistry,* **46** 2105-2127 (2022).

21. B. Vaghefinazari, E. Wierzbicka, P. Visser, R. Posner, R. Arrabal, E. Matykina, M. Mohedano, C. Blawert, M. L. Zheludkevich, and S. V. Lamaka, *Materials,* **15** (23), 8489 (2022).

22. S. Ono, *Journal of the Surface Finishing Society of Japan.* **62** 198-203 (2011).

23. J. H. Nordlien, K. Nisancioglu, S. Ono, and N. Masuko, *Journal of the Electrochem Society.,* **144** (2), 461-466 (1997).

24. J. H. Nordlien, K. Nisancioglu, S. Ono, and N. Masuko, *Journal of the Electrochem Society,* **143** (8), 2564-2572 (1996).

25. S. Ono, H. Kijima, and N. Masuko, *Materials Transactions,* **44** (4), 539-545 (2003).

26. T. Uchikoshi, H. Takahashi, N. Shirahata, and Y. Sakka, *Journal of the Ceramic Society of Japan,* **115** (1348), 818-820 (2007).

27. T. Uchikoshi, *Journal of the Society of Inorganic Materials, Japan,* **8** 478-483 (2001).

28. S. Heise, M. Hohlinger, Y. T. Hernandez, J. J. P. Palacio, J. A. R. Ortiz, V. Wagener, S. Virtanen, and A. R. Boccaccini, *Electrochimica Acta,* **232** 456-464 (2017).

29. S. Hiromoto and K. Doi, *Materials Transactions,* **64** (5), 1011-1019 (2023).

30. S. Hiromoto and K. Doi, *in* "Annual Meeting of Japan Institute of Metals and Materials", Vol. 170, Online, 2022.

31. T. Yamagishi, Y. Oyanagi, and E. Narita, Nippon Kagaku Kaishi*,* **1993** (4), 329-334 (1993).

32. M. Iida, K. Yoshikawa, M. Togo, and A. Nakahira, *Journal of the Japan Society of Powder Powder Metallurgy,* **64** (11), 595-600 (2017).

33. T. Sato, *Journal of the Mineralogical Society of Japan,* **19** (1), 21-41 (1989).

34. S. J. Palmer, L. M. Grand, and R. L. Frost, *Spectrochimica Acta Part A: Molecular and Biomolecular Spectroscopy,* **79** (1), 156-160 (2011).

35. R. L. Frost, R. Scholz, A. Lopez, and F. L. Theiss, *Spectrochimica Acta Part A: Molecular and Biomolecular Spectroscopy,* **118** 187-191 (2014).

36. M. Mora, C. Jimenez-Sanchidrian, and J. R. Ruiz, *Materials Letters,* **120** 193-195 (2014).

37. J. T. Kloprogge, D. Wharton, L. Hickey, and R. L. Frost, *American Mineralogist,* **87** 623-629 (2002).

38. R. Sasai, T. Fujimura, H. Sato, E. Nii, M. Sugata, Y. Nakayashiki, H. Hoashi, C. Moriyoshi, E. Oishi, Y.

Fujii, S. Kawaguchi, and H. Tanaka, *Bulletin of the Chemical Society of Japan.,* **95** (5), 802-812 (2022).

39. L. Jinlong, L. Hongyun, and X. Jinpeng, *Applied Surface Science,* **273** 192-198 (2013).

40. N. J. Cherepy, T. H. Shen, A. P. Esposito, and T. M. Tillotson, *Journal of Colloid and Interface Science,* **282** (1), 80-86 (2005).

41. R. L. Frost, S. Bahfenne, and J. Graham, *Journal of Raman Spectroscopy,* **40** (8), 855-860 (2009).

42. Z. P. Xu and H. C. Zeng, *Journal of Physical Chemistry B*, 105 (9), 1743-1749 (2001).

43. V. R. L. Constantino and T. J. Pinnavaia, Inorg. Chem., 34, 883-892 (1995).

44. H. Hirahara, Y. Sawai, S. Aisawa, S. Takahashi, Y. Umetsu, and E. Narita, *Journal of the Clay Science Society of Japan,* **42** (2), 70-76 (2002).

45. F. Cavani, F. Trifiro, and A. Vaccari, *Catalysis Today,* **11** (2), 173-301 (1991).

46. S. Miyata, *Clays and Clay Minerals,* **31** (4), 305-311 (1983).

Table and Figure Captions

Table 1. Corrosion parameters obtained by curve fitting using equivalent electric circuits shown in Fig. 8(c) and (d).

Figure 1. (a)-(d) Optical images of AZ31 immersed in 0.1 mol/L NaCl solution supplemented with (a) 0 mmol/L, (b) 1 mmol/L, (c) 10 mmol/L, and (d) 50 mmol/L $NaAlO_2$. (e) SEM image of AZ31 immersed with 50 mmol/L $NaAlO_2$.

Figure 2. (a) Weight gain of AZ31 after immersion in 0.1 mol/L NaCl solution supplemented with and without $NaAlO_2$ and (b) pH of the solution before and after immersion of AZ31.

Figure 3. (a) XPS survey spectra obtained from surface of AZ31 immersed in 0.1 mol/L NaCl solution with 10 and 50 mmol/L $NaAlO_2$ and as-polished AZ31. XPS narrow spectra of (b) C 1s, (c) O 1s, (d) Al 2p, (e) Mg 2p and (f) Zn 2p3 regions of (i) AZ31 immersed with 50 mmol/L $NaAlO_2$, and (ii) AZ31 immersed with 10 mmol/L $NaAlO_2$ and (iii) as-polished AZ31.

Figure 4. (a) Cathodic and (b) anodic polarization curves of AZ31 in 0.1 mol/L NaCl solution supplemented with (i) 0mmol/L, (ii) 10 mmol/L and (iii) 50 mmol/L $NaAlO_2$.

Figure 5. (a) Wide range XRD patterns and (b) magnified $(003)_{LDH}$ peak of (i) as-synthesized and (ii) 140°C-treated $LDHAlO_2$ particles and (iii) as-received and (iv) 140°C-treated $LDHCO_3$ particles.

Figure 6. (a) and (b) Optical and (c)-(j) SEM images of (a), (c), (e), (g) and (i) $LDHAlO_2$-coated and (b), (d), (f), (h) and (j) $LDHCO_3$-coated AZ31 formed by EP-co-D followed by ultrasonication. (c) and (d) low magnification surface images, high magnification surface images of (e) and (f) coating and (g) and (h) substrate exposed in a crack in coating, and (i) and (j) cross-section images.

Figure 7. (a) Wide range XRD patterns and (b) magnified $(003)_{LDH}$ peak of (i) $LDHAlO_2$-

coated and (ii) $LDHCO_3$-coated AZ31 formed by EP-co-D followed by ultrasonication.

Figure 8. (a) Anodic polarization curves and (b) Nyquist and (c) Bode plots of EI spectra of $LDHAlO_2$-coated, $LDHCO_3$-coated and uncoated AZ31 in 0.1 mol/L NaCl solution. Assumed equivalent electric circuits for (d) $LDHAlO_2$- and $LDHCO_3$-coated AZ31 and (e) uncoated AZ, and (f) R_p values obtained by curve fitting.

Figure 9. Weight gain of $LDHAlO_2$-coated, $LDHCO_3$-coated and uncoated AZ31 after wet-dry cyclic corrosion tests.

Figure 10. (a)-(f) Optical (g)-(l) SEM images of $LDHAlO_2$-coated, $LDHCO_3$-coated and uncoated AZ31 after wet-dry corrosion tests. (a), (d), (g), (i) and (k) $LDHAlO_2$-coated, (b), (e), (h), (j) and (l) $LDHCO_3$-coated and (c) and (f) uncoated AZ31. (b), (e) and (f) are magnified images of arrowed area on (a), (b) and (c) images, respectively. (g) and (h) magnified images of a corrosion area. (i) and (j) magnified images of coating in apparently uncorroded area. (k) and (l) cross-section images.

Figure 11. (a) Wide range XRD patterns and (b) magnified $(003)_{LDH}$ peak of (i) $LDHAlO_2$-coated, (ii) $LDHCO_3$-coated and (iii) uncoated AZ31 after wet-dry cyclic corrosion tests.

Figure 12. Raman spectra of (a) $LDHAlO_2$ and (b) $LDHCO_3$ coatings (i) before and (ii) after wet-dry cyclic corrosion tests.

Figure 13. (a) and (b) Optical images, (c) and (d) SEM images of corroded areas indicated by an arrow on the optical images, and (e) and (f) topography images corresponding to (a) and (b) images. (g)-(i) Profiles of line 1)-3) on images (e) and (f). (a), (c), (e) and (g) $LDHAlO_2$-coated AZ31 and (b), (d), (f), (h) and (i) $LDHCO_3$-coated AZ31 after wet-dry cyclic corrosion tests, after removing corrosion product and coating layer.

Figure 14. Assumed corrosion mechanisms of (a) $LDHAlO_2$- and (b) $LDHCO_3$-coated AZ31 in wet-dry corrosion environment.

Table 1. Corrosion parameters obtained by curve fitting using equivalent electric circuits shown in Fig. 8(c) and (d).

	R_s / Ω·cm^2	R_{coat} or R_{film} / kΩ·cm^2	CPE_{coat}-T or CPE_{film}-T / μF s^{P-1}·cm^2	CPE_{coat}-P or CPE_{film}-P / -	R_{ct} / kΩ·cm^2	CPE_{dl}-T / mF s^{P-1}·cm^2	CPE_{dl}-P / -	R_p / kΩ·cm^2
LDHAlO$_2$-coated AZ31	53 ± 2.6	8.6 ± 0.5	8.1 ± 0.9	0.94 ± 0.00	-	-	-	8.6 ± 0.5
LDHCO$_3$-coated AZ31	41 ± 2.1	11 ± 1.4	12 ± 4.1	0.91 ± 0.04	-	-	-	11.0 ± 1.4
Uncoated AZ31	47 ± 3.8	2.1 ± 0.4	9.6 ± 1.0	0.94 ± 0.00	0.98±0.17	1.1±0.2	0.80±0.01	3.0±0.6

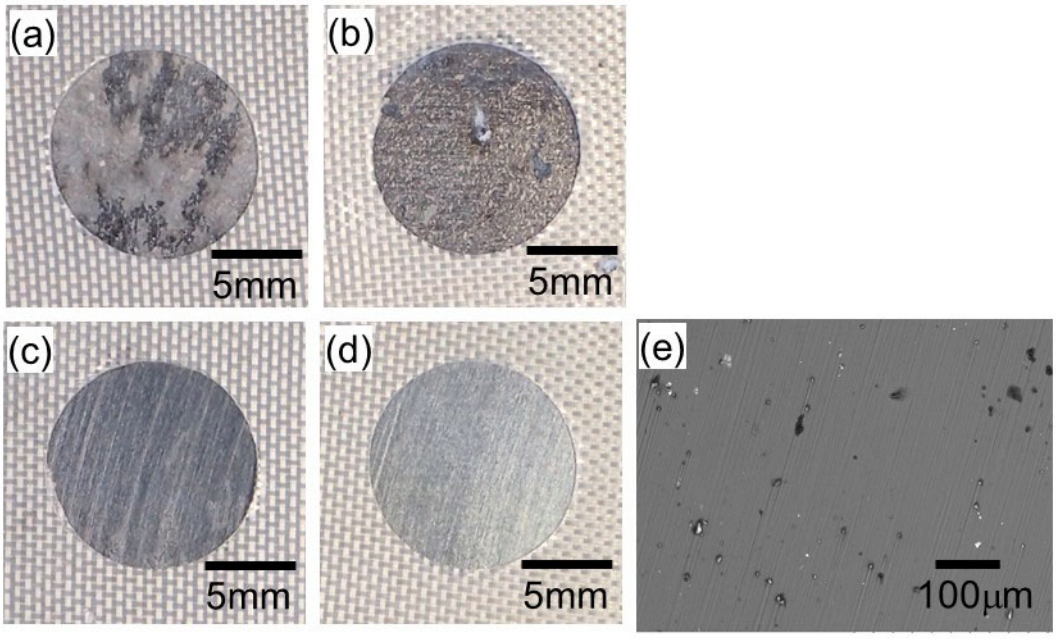

Figure 1. (a)-(d) Optical images of AZ31 immersed in 0.1 mol/L NaCl solution supplemented with (a) 0 mmol/L, (b) 1 mmol/L, (c) 10 mmol/L, and (d) 50 mmol/L $NaAlO_2$. (e) SEM image of AZ31 immersed with 50 mmol/L $NaAlO_2$.

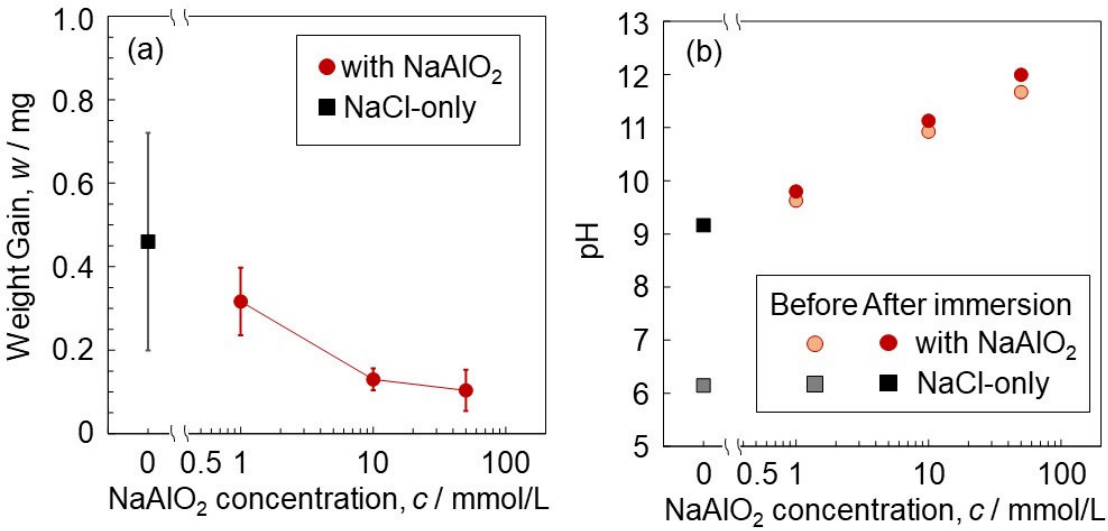

Figure 2. (a) Weight gain of AZ31 after immersion in 0.1 mol/L NaCl solution supplemented with and without $NaAlO_2$ and (b) pH of the solution before and after immersion of AZ31.

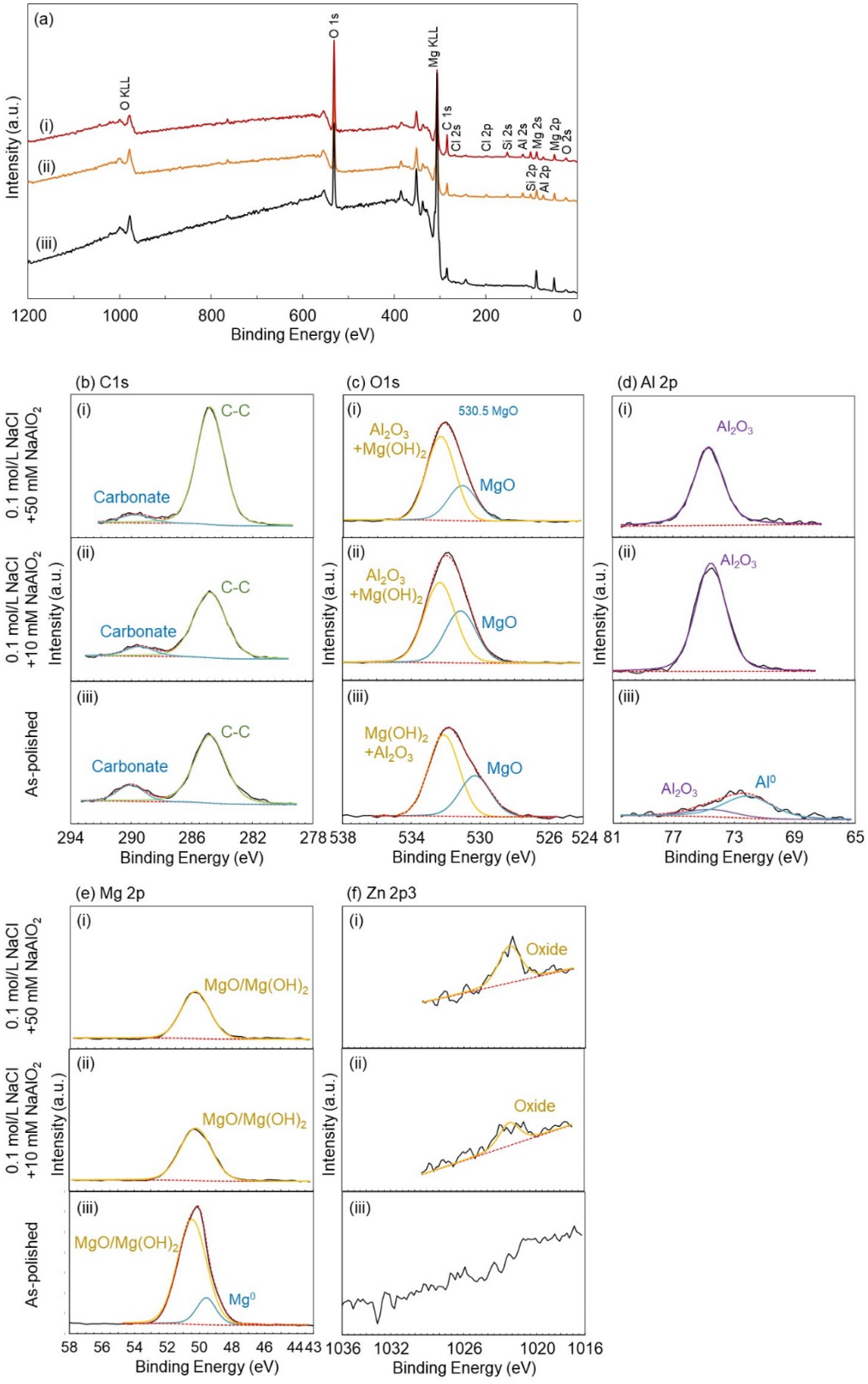

Figure 3. (a) XPS survey spectra obtained from surface of AZ31 immersed in 0.1 mol/L NaCl solution with 10 and 50 mmol/L $NaAlO_2$ and as-polished AZ31. XPS narrow spectra of (b) C 1s, (c) O 1s, (d) Al 2p, (e) Mg 2p and (f) Zn 2p3 regions of (i) AZ31 immersed with 50 mmol/L $NaAlO_2$, and (ii) AZ31 immersed with 10 mmol/L $NaAlO_2$ and (iii) as-polished AZ31.

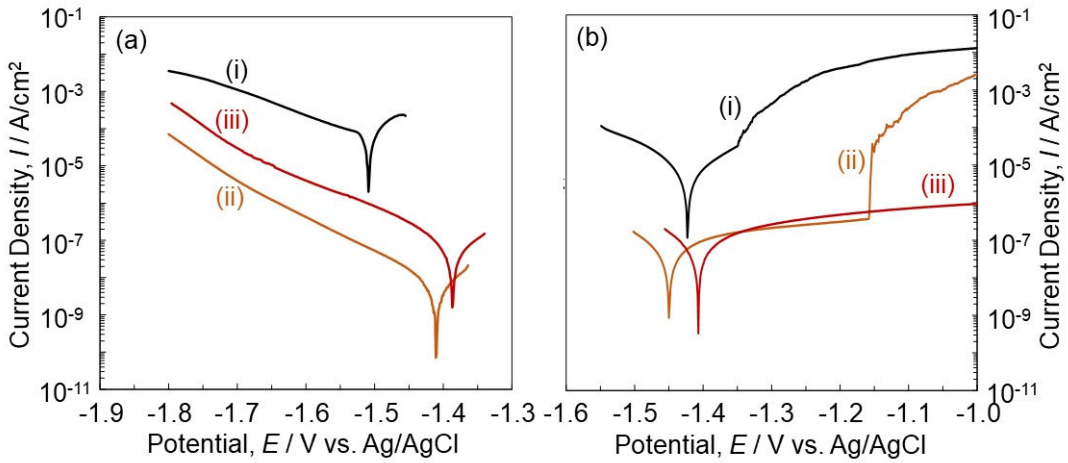

Figure 4. (a) Cathodic and (b) anodic polarization curves of AZ31 in 0.1 mol/L NaCl solution supplemented with (i) 0 mmol/L, (ii) 10 mmol/L and (iii) 50 mmol/L $NaAlO_2$.

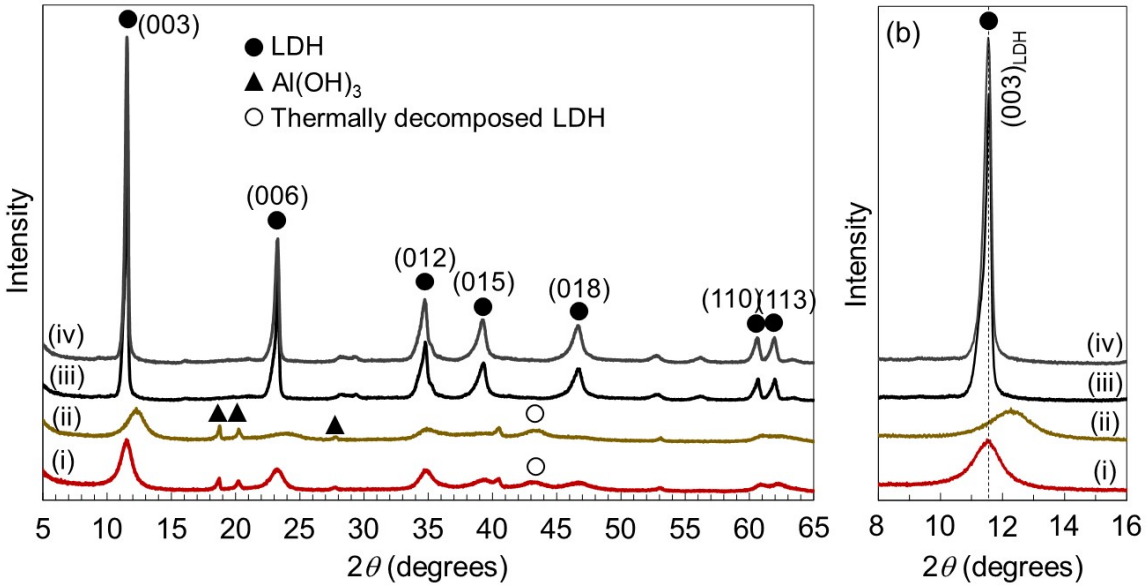

Figure 5. (a) Wide range XRD patterns and (b) magnified $(003)_{LDH}$ peak of (i) as-synthesized and (ii) 140°C-treated LDHAlO_2 particles and (iii) as-received and (iv) 140°C-treated LDHCO_3 particles.

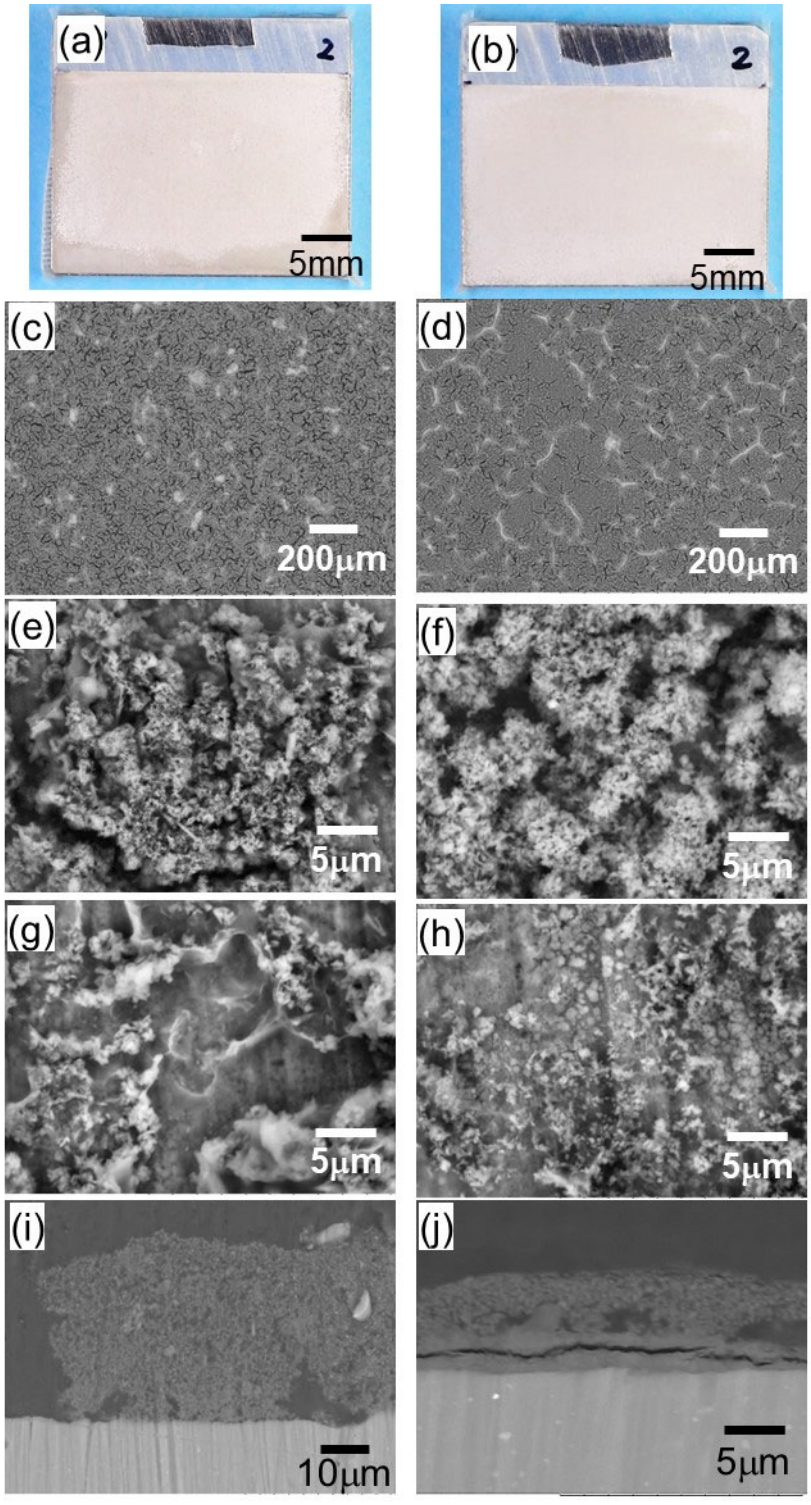

Figure 6. (a) and (b) Optical and (c)-(j) SEM images of (a), (c), (e), (g) and (i) LDHAlO$_2$-coated and (b), (d), (f), (h) and (j) LDHCO$_3$-coated AZ31 formed by EP-co-D followed by ultrasonication. (c) and (d) low magnification surface images, high magnification surface images of (e) and (f) coating and (g) and (h) substrate exposed in a crack in coating, and (i) and (j) cross-section images.

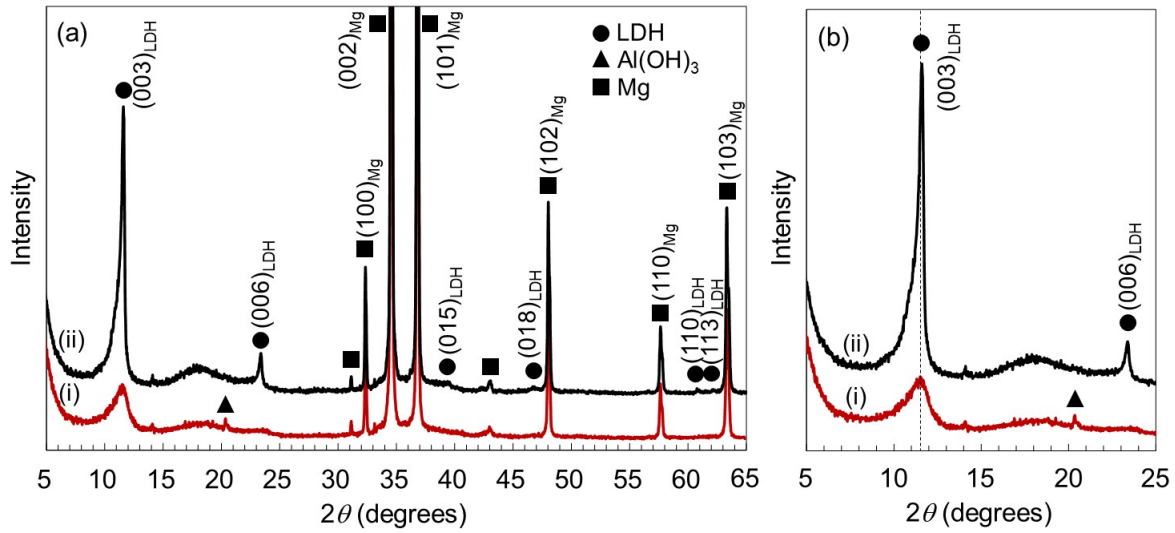

Figure 7. (a) Wide range XRD patterns and (b) magnified $(003)_{LDH}$ peak of (i) $LDHAlO_2$-coated and (ii) $LDHCO_3$-coated AZ31 formed by EP-co-D followed by ultrasonication.

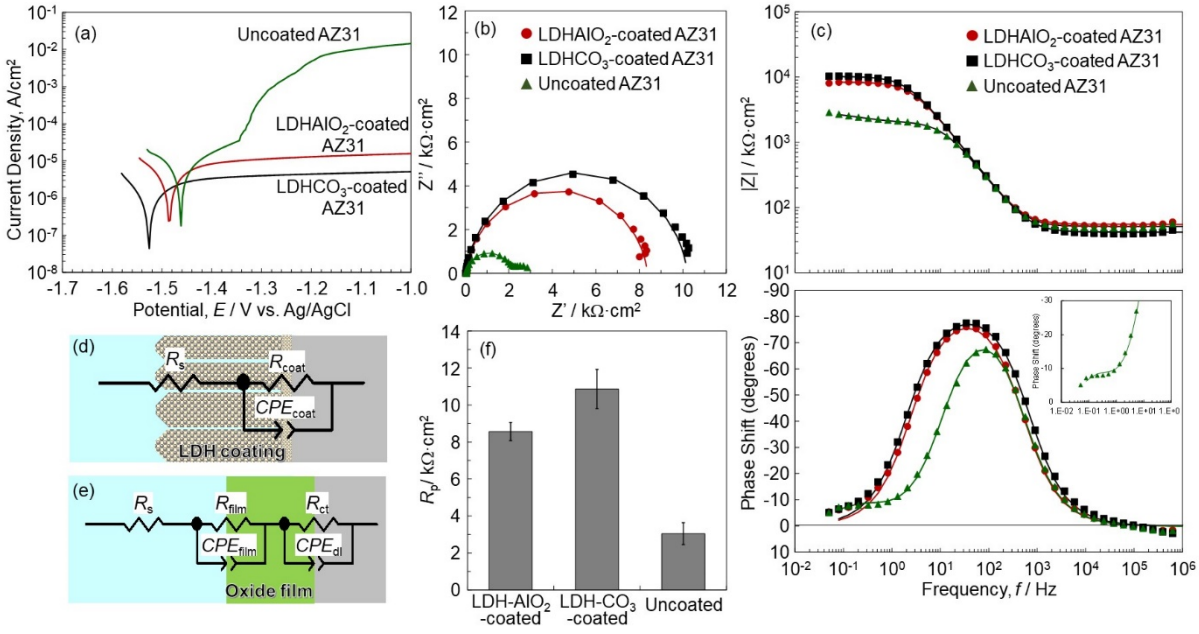

Figure 8. (a) Anodic polarization curves and (b) Nyquist and (c) Bode plots of EI spectra of $LDHAlO_2$-coated, $LDHCO_3$-coated and uncoated AZ31 in 0.1 mol/L NaCl solution. Assumed equivalent electric circuits for (d) $LDHAlO_2$- and $LDHCO_3$-coated AZ31 and (e) uncoated AZ, and (f) R_p values obtained by curve fitting.

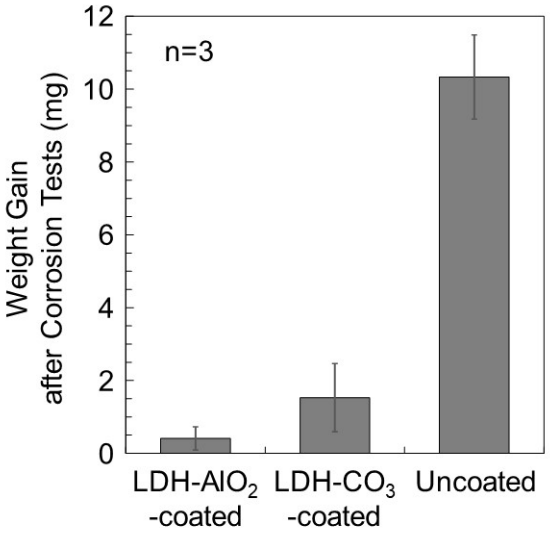

Figure 9. Weight gain of $LDHAlO_2$-coated, $LDHCO_3$-coated and uncoated AZ31 after wet-dry cyclic corrosion tests.

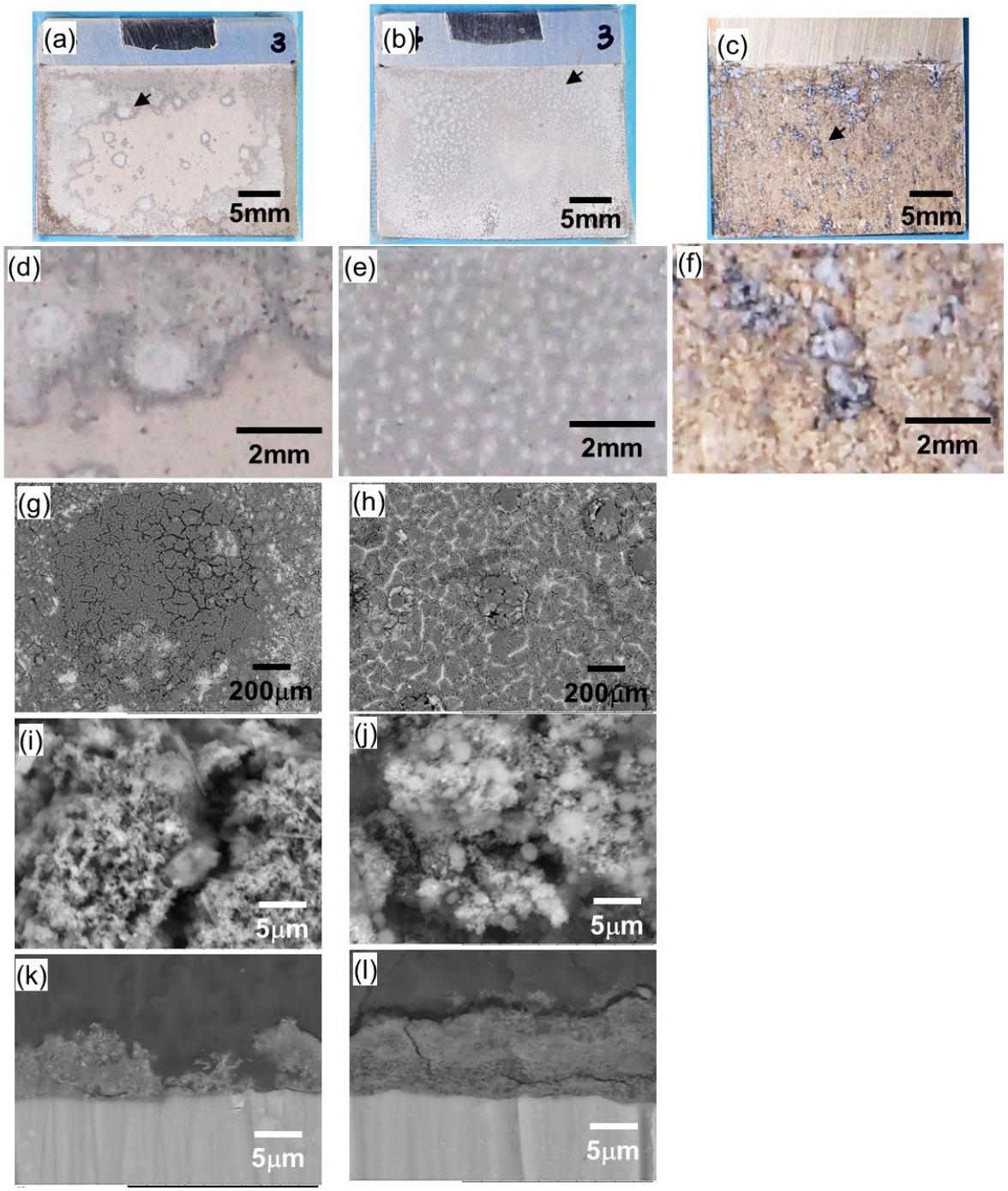

Figure 10. (a)-(f) Optical (g)-(l) SEM images of $LDHAlO_2$-coated, $LDHCO_3$-coated and uncoated AZ31 after wet-dry corrosion tests. (a), (d), (g), (i) and (k) $LDHAlO_2$-coated, (b), (e), (h), (j) and (l) $LDHCO_3$-coated and (c) and (f) uncoated AZ31. (b), (e) and (f) are magnified images of arrowed area on (a), (b) and (c) images, respectively. (g) and (h) magnified images of a corrosion area. (i) and (j) magnified images of coating in apparently uncorroded area. (k) and (l) cross-section images.

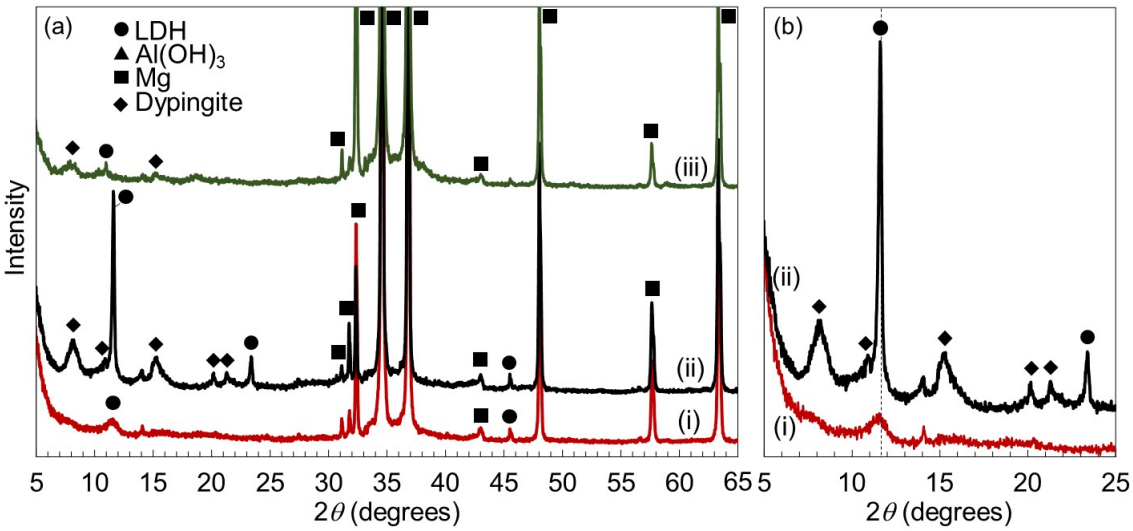

Figure 11. (a) Wide range XRD patterns and (b) magnified $(003)_{LDH}$ peak of (i) $LDHAlO_2$-coated, (ii) $LDHCO_3$-coated and (iii) uncoated AZ31 after wet-dry cyclic corrosion tests.

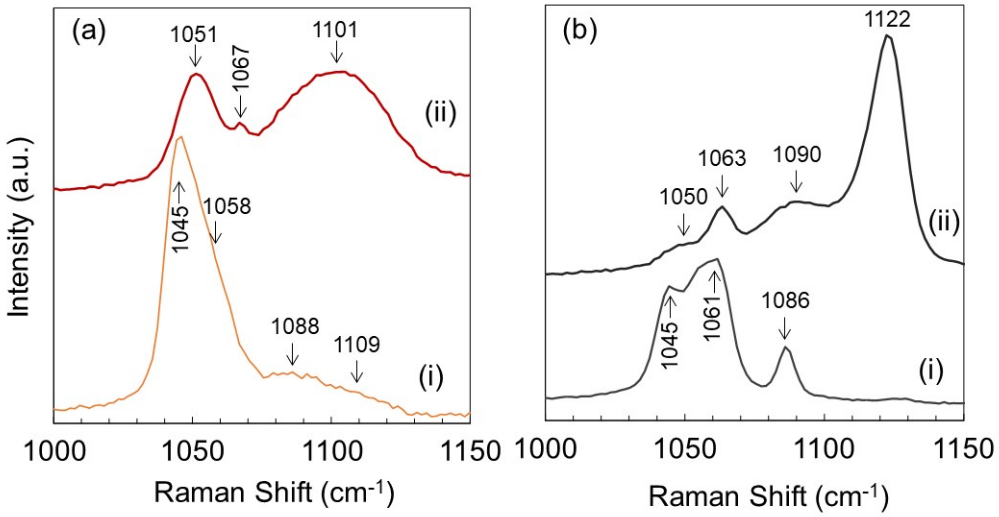

Figure 12. Raman spectra of (a) $LDHAlO_2$ and (b) $LDHCO_3$ coatings (i) before and (ii) after wet-dry cyclic corrosion tests.

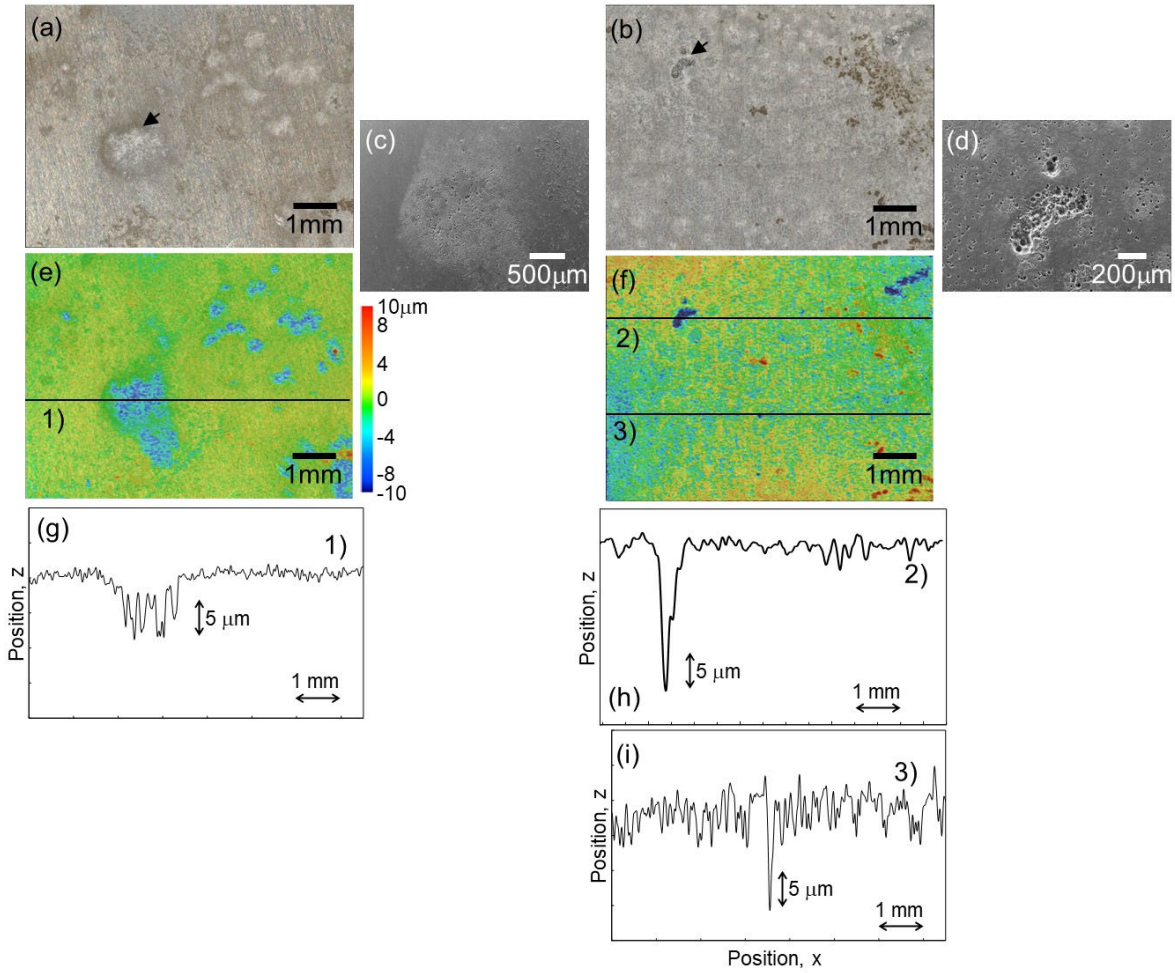

Figure 13. (a) and (b) Optical images, (c) and (d) SEM images of corroded areas indicated by an arrow on the optical images, and (e) and (f) topography images corresponding to (a) and (b) images. (g)-(i) Profiles of line 1)-3) on images (e) and (f). (a), (c), (e) and (g) $LDHAlO_2$-coated AZ31 and (b), (d), (f), (h) and (i) $LDHCO_3$-coated AZ31 after wet-dry cyclic corrosion tests, after removing corrosion product and coating layer.

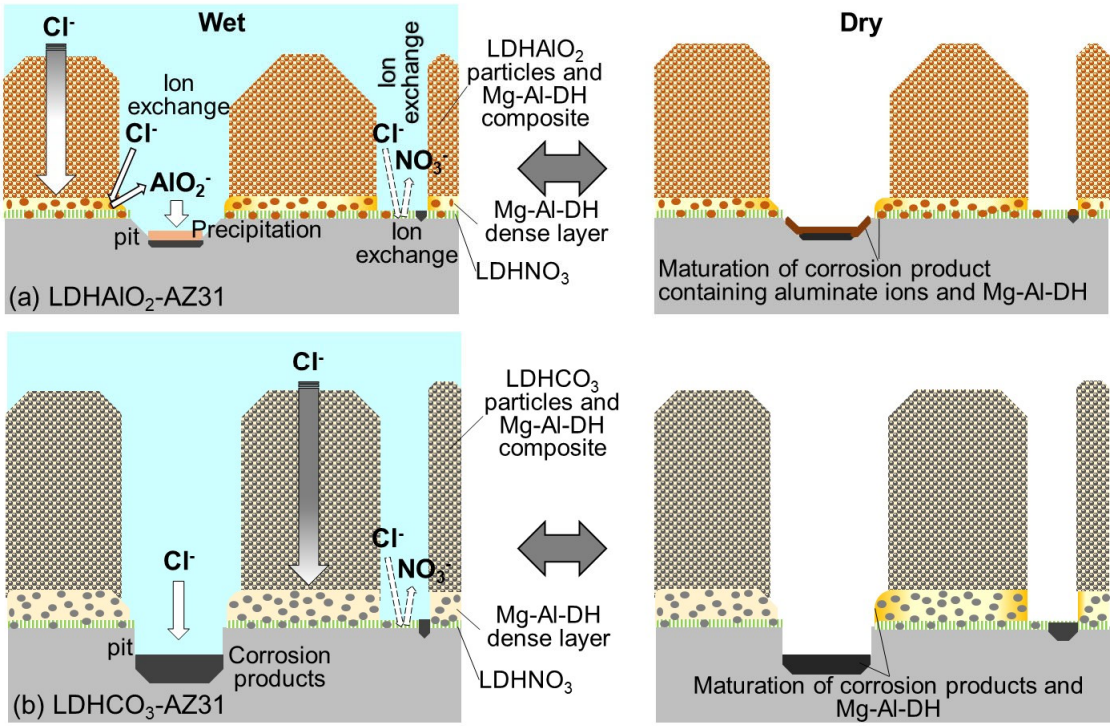

Figure 14. Assumed corrosion mechanisms of (a) $LDHAlO_2$- and (b) $LDHCO_3$-coated AZ31 in wet-dry corrosion environment.